View metadata, citation and similar papers at core.ac.uk
brought to you by CORE
provided by Ghent University Academic Bibliography

NUMERICAL AND EXPERIMENTAL STUDY ON THE WAVE–BODY INTERACTION PROBLEM WITH THE EFFECT OF FORWARD SPEED AND FINITE WATER DEPTH IN REGULAR WAVES

Tianlong Mei, School of Naval Architecture, Ocean and Civil Engineering, Shanghai Jiao Tong University, China; Maritime Technology Division, Ghent University, Belgium
Guillaume Delefortrie, Flanders Hydraulics Research and Maritime Technology Division, Ghent University, Belgium
Manasés Tello Ruiz, **Changyuan Chen, Evert Lataire** and **Marc Vantorre**, Maritime Technology Division, Ghent University, Belgium
Zaojian Zou, State Key Laboratory of Ocean Engineering, Shanghai Jiao Tong University, China; School of Naval Architecture, Ocean and Civil Engineering, Shanghai Jiao Tong University, China

SUMMARY

In this study, a time domain higher-order Rankine panel method is developed and applied to solve the wave–body interaction problem in regular waves. The hydrodynamic effects of forward speed and finite water depth are accounted for. In order to verify the proposed numerical method, the Duisburg Test Case (DTC) containership is chosen as a case study. The numerical results for the wave induced ship's motions and the added resistance will be validated against model tests, which were carried out in the Towing Tank for Manoeuvres in Confined Water at Flanders Hydraulics Research (FHR) in cooperation with Ghent University (UGent) as part of the SHOPERA project.

1 INTRODUCTION

With more and more deep drafted ships navigating or manoeuvring near shore or in coastal areas, it is desired to have a better insight in the effects of shallow water. Shallow water would lead to a more complicated hydrodynamic behaviours compared to the open sea. What is more, these areas are often subjected to wave conditions. In fact, under the presence of waves in shallow water areas, not only the safety related issues of the manoeuvring ship should arouse concern, but also the seakeeping behaviour, such as wave-induce motions and added resistance, needs to be taken into account to avoid grounding and to quantify speed reduction. Hence, it is essential to investigate the wave-induced motions and second order forces in finite water depth.

For this reason, many researchers have focused on the corresponding numerical scheme of wave body interaction problems in finite water depths. In an early stage, the 2D strip method was used for its practicability and high efficiency in the initial design, see e.g. (Kim, 1968; Hwang and Lee, 1975; Takaki, 1977; Takaki et al. 1978; Andersen, 1979; Perunovic and Jensen, 2003; Kim, 1999; Kim and Kim, 2012; Vantorre and Journée, 2003). The mentioned method, however, is only suitable for relatively high frequencies and a slender body ship hull. Because of this limitation, researchers turned their attention to the matched asymptotic expansion method (MAEM), which performed matching of solutions on the interface boundary by using different numerical techniques on the divided field zones, e.g. (Tuck, 1970; Vorobyov and Stasenko, 2010). The main problem with this method is that because of the long wave assumption large deviations found when the wave length is close to the ship length.

More advance techniques, available nowadays, such as the Green function based 3D panel method and the Rankine source based 3D panel method. The free surface Green function based 3D panel method has been initially applied by researchers, e.g. (Oortmerssen, 1976; Chan, 1990; Li, 2001). Though the accuracy seems to be better than the 2D method or MAEM, the form and evaluation of Green function is relatively complex and difficult. Furthermore, the Neumann-Kelvin linearization of the method cannot consider the interaction between steady and unsteady flow. In comparison, the Rankine source based 3D panel method has been widely used for its flexible treatment of the free surface as well as the simpler kernel form (Söding et al., 2014; Riesner et al., 2016; Riesner and Moctar, 2018). Gao et al., 2008and Yao et al., 2017, among others, applied the Rankine panel method for shallow water conditions, in the frequency domain. In their method, however, the coupling effect with the nonlinear external force cannot be considered (Kim and Kim, 2012). The time domain Rankine panel method is applied for the wave induced motion problems in shallow water, e.g. (Kim and Kim, 2012; Kim and Kim, 2013; Feng et al., 2016; Wang et al., 2016), but their studies only focus on the zero forward speed cases.

In the present study, a time domain higher-order Rankine panel method is developed to investigate the motion responses and added resistance of a moving ship in various water depths in regular waves. The image method is used to satisfy the bottom boundary condition. A good agreement is achieved when comparing the numerical results with the model tests which were executed in the Towing Tank for Manoeuvres in Confined Water at Flanders Hydraulics Research in cooperation with Ghent University as part of the SHOPERA project.

2 MATHEMATICAL FORMULATION

2.1 BOUNDARY VALUE PROBLEM OF RANKINE PANEL METHOD

In the frame of potential theory, a coordinate system $o-xyz$ fixed to a ship with the forward speed U_0 is introduced as shown in Figure 1. Then the total velocity potential $\Psi(\vec{x},\mathrm{t})$ can be written as,

$$\Psi(\vec{x},\mathrm{t}) = \phi_s(\vec{x}) + \varphi_I(\vec{x},\mathrm{t}) + \varphi_d(\vec{x},\mathrm{t}) \quad (1)$$

where ϕ_s, φ_I and φ_d are the basic velocity potential, the regular incoming wave potential and the disturbance velocity potential respectively.

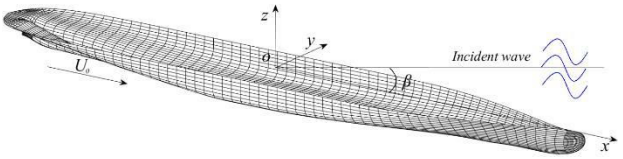

Figure 1. Coordinate system.

Similarly, the wave elevation $\zeta(\vec{x},\mathrm{t})$ can be written as,

$$\zeta(\vec{x},\mathrm{t}) = \zeta_I(\vec{x},\mathrm{t}) + \zeta_d(\vec{x},\mathrm{t}) \quad (2)$$

Naturally, the regular incoming wave potential $\varphi_I(\vec{x},\mathrm{t})$ is given as follows,

$$\varphi_I(\vec{x},t) = \frac{\zeta_A g}{\omega}\frac{\cosh[k(z+h)]}{\cosh kh} sin[k(xcos\beta + ysin\beta) - \omega_e t] \quad (3)$$

where ζ_A is the wave amplitude, ω the wave natural frequency, β the wave angle and k the wave number. The dispersion relation in finite water depth (Figure 2) is:

$$\omega^2 = kgtanh(kh) \quad (4)$$

ω_e is the encounter frequency defined as:

$$\omega_e = \omega - kU_0 cos\beta \quad (5)$$

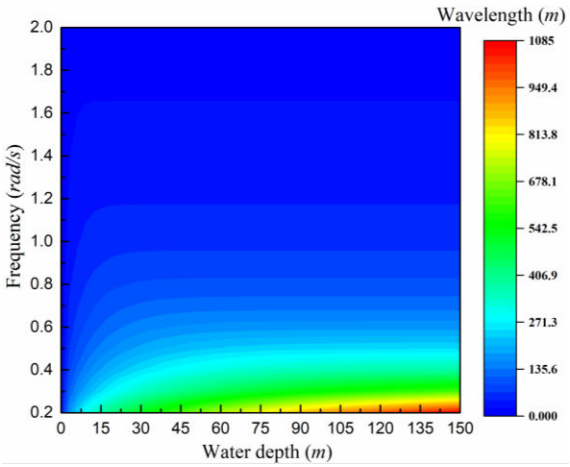

Figure 2. The dispersion relation in finite water depth.

The velocity $\Psi(\vec{x},\mathrm{t})$ satisfies the following boundary value problem (BVP),

$$\nabla^2\Psi = 0, \text{ in the fluid domain} \quad (6)$$

The kinematic and dynamic free surface conditions on the free surface $\mathrm{z} = \zeta(x,y,t)$:

$$\left[\frac{\partial}{\partial \mathrm{t}} - \left(\vec{U} - \nabla\Psi\right)\cdot\nabla\right]\left(\mathrm{z} - \zeta(x,y,t)\right) = 0 \quad (7)$$

$$\left[\frac{\partial}{\partial \mathrm{t}} - \left(\vec{U} - \nabla\Psi\right)\cdot\nabla\right]\Psi = -g\zeta + \frac{1}{2}\nabla\Psi\cdot\nabla\Psi \quad (8)$$

$$\frac{\partial\Psi}{\partial n} = U_0 n_1 + \frac{\partial\vec{\delta}}{\partial t}\cdot\vec{n}, \text{ on body surface } S_b \quad (9)$$

$$\frac{\partial\Psi}{\partial n} = 0, \text{ on the seabed } z = -h \quad (10)$$

where $\vec{\delta}$ is wave induced motion vector and can be written as $\vec{\delta} = \vec{\xi}_T + \vec{\xi}_R \times \vec{r}$, translation vector $\vec{\xi}_T = (\xi_1,\xi_2,\xi_3)$, rotation vector $\vec{\xi}_R = (\xi_4,\xi_5,\xi_6)$.

In present study, the double body linearization is used. By submitting Eq. (1) in Eq. (6) - Eq. (10), the linearized BVP of $\varphi_d(\vec{x},\mathrm{t})$ can be derived as follows,

$\nabla^2\varphi_d = 0$, in the fluid domain;

The kinematic and dynamic free surface conditions on the free surface $\mathrm{z} = 0$

$$\left[\frac{\partial}{\partial \mathrm{t}} - \left(\vec{U} - \nabla\phi_s\right)\cdot\nabla\right]\zeta_d = \frac{\partial\varphi_d}{\partial \mathrm{z}} + \frac{\partial^2\varphi_d}{\partial \mathrm{z}^2}\zeta - \nabla\phi_s\cdot\nabla\zeta_I \quad (11)$$

$$\left[\frac{\partial}{\partial \mathrm{t}} - \left(\vec{U} - \nabla\phi_s\right)\cdot\nabla\right]\varphi_d = -g\zeta_d - \nabla\phi_s\cdot\nabla\zeta_I + \vec{U}\cdot\nabla\phi_s - \frac{1}{2}\nabla\phi_s\cdot\nabla\phi_s \quad (12)$$

$$\frac{\partial\varphi_d}{\partial n} = \sum_{j=1}^{6}(\dot{\xi}_j n_j + \xi_j m_j) - \frac{\partial\varphi_I}{\partial n}, \text{ on mean body surface } \vec{S}_b \quad (13)$$

$$\frac{\partial\varphi_d}{\partial n} = 0, \text{ on the seabed } z = -h \quad (14)$$

$$\varphi_d = 0, \partial\varphi_d/\partial t = 0 \text{ at } t = 0 \quad (15)$$

where $m_j, j = 1\sim6$ represents the interaction between steady and unsteady flows, defined as:

$$\begin{aligned}(m_1,m_2,m_3) &= (\vec{n}\cdot\nabla)\left(\vec{U} - \nabla\phi_s\right)\\ (m_4,m_5,m_6) &= (\vec{n}\cdot\nabla)[\vec{x}\times\left(\vec{U} - \nabla\phi_s\right)]\end{aligned} \quad (16)$$

The detailed evaluation of the m_j term can be found in Mei et al..

2.2 EQUATIONS OF SHIP MOTIONS AND FORCES

The 6-DOF ship motion equations can be obtained based on Newton's Second Law,

$$M_{ij}\ddot{\xi}_j(t) + C_{ij}\xi_j(t) = F_i\left(\dot{\xi}_j, \xi_j, t\right), \quad i,j = 1\sim6 \tag{17}$$

where M_{ij} and C_{ij} represent mass and restoring coefficients matrix, respectively.

The hydrodynamic forces and moments $F_i\left(\dot{\xi}_j, \xi_j, t\right)$ can be evaluated by,

$$F_i = -\iint_{\vec{S}_b} \rho[\frac{\partial}{\partial t} - \left(\vec{U} - \nabla\phi_s\right)\cdot\nabla]\,\varphi_{I,d} n_i ds, i = 1\sim6 \tag{18}$$

For a harmonic forced ship, the radiation force F_{ij} can be expressed as:

$$\begin{aligned} F_{ij} &= -\left[A_{ij}(\omega_e)\ddot{\bar{\xi}}_j(t) + B_{ij}(\omega_e)\dot{\bar{\xi}}_j(t)\right] \\ &= \left[\omega_e^2 A_{ij}(\omega_e) - i\omega_e B_{ij}(\omega_e)\right]\bar{\xi}_j e^{i\omega_e t} \end{aligned} \tag{19}$$

where ω_e and $\bar{\xi}_j$ are the harmonic forced motion frequency and amplitude, respectively.

Then the added mass and damping coefficient can further be obtained by:

$$\begin{aligned} A_{ij} &= \frac{Re(F_{ij})}{\omega_e^2 \bar{\xi}_j} \\ B_{ij} &= \frac{Im(F_{ij})}{\omega_e \bar{\xi}_j} \end{aligned} \tag{20}$$

In this study, the added wave resistance is evaluated by applying the pressure integration method (also known as near field method) proposed by Joncquez (2009),

$$\begin{aligned} \vec{F}^{(2)} &= -\rho\iint_{\vec{S}_b} \nabla\left(\frac{\partial}{\partial t} - \left(\vec{U} - \nabla\phi_s\right)\cdot\nabla\varphi\right)\cdot\vec{\delta}\,\vec{n}_0 ds \\ &-\rho\iint_{\vec{S}_b} \vec{H}\vec{x}\cdot\nabla\left(\vec{U}\cdot\nabla\phi_s + \frac{1}{2}\nabla\phi_s\cdot\nabla\phi_s + gz\right)\vec{n}_0 ds \\ &-\rho\iint_{\vec{S}_b} \frac{1}{2}\nabla\varphi\cdot\nabla\varphi\,\vec{n}_0 ds \\ &-\rho\iint_{\vec{S}_b} \left[\frac{\partial\varphi}{\partial t} - \vec{U}\cdot\nabla\varphi + \nabla\phi_s\cdot\nabla\varphi + g(\xi_3 + \xi_4 y - \xi_5 x)\right]\cdot\vec{n}_1 ds \\ &-\rho\iint_{\vec{S}_b} \left[\nabla\left(-\vec{U}\cdot\nabla\phi_s + \frac{1}{2}\nabla\phi_s\cdot\nabla\phi_s\right)\right]\vec{\delta}\vec{n}_1 ds \\ &-\rho\iint_{\vec{S}_b} \left(-\vec{U}\cdot\nabla\phi_s + \frac{1}{2}\nabla\phi_s\cdot\nabla\phi_s + gz\right)\vec{H}\,\vec{n}_2 ds \\ &+\frac{1}{2}\rho g\int_{wl}[\zeta - (\xi_3 + \xi_4 y - \xi_5 x)]^2\frac{\vec{n}_0}{sin\alpha}dl \\ &-\rho\int_{wl}\left[-\vec{U}\cdot\nabla\phi_s + \frac{1}{2}\nabla\phi_s\cdot\nabla\phi_s\right][\zeta - (\xi_3 + \xi_4 y - \xi_5 x)]\frac{\vec{n}_1}{sin\alpha}dl \end{aligned} \tag{21}$$

where $\varphi = \varphi_I(\vec{x}, t) + \varphi_d(\vec{x}, t)$, the wave induced motion vector is $\vec{\delta} = \vec{\xi}_T + \vec{\xi}_R \times \vec{x}$, and the vectors $\vec{n}_0$, $\vec{n}_1$ and $\vec{n}_2$ mean the zero, first and second-order components of the normal vector on the hull surface, $\vec{H}$ is second-order transformation matrix. α represents the angle of the hull flare at free surface.

$$\vec{n}_0 = \begin{Bmatrix} \vec{n} \\ \vec{x}\times\vec{n} \end{Bmatrix}; \vec{n}_1 = \begin{Bmatrix} \vec{\xi}_R\times\vec{n} \\ \vec{\xi}_T\times\vec{n} + \vec{\xi}_R\times(\vec{x}\times\vec{n}) \end{Bmatrix};$$

$$\vec{n}_2 = \begin{Bmatrix} \vec{H}\vec{n} \\ \vec{H}(\vec{x}\times\vec{n}) + \vec{\xi}_T\times(\vec{\xi}_R\times\vec{n}) \end{Bmatrix};$$

$$\vec{H} = \frac{1}{2}\begin{bmatrix} -(\xi_5^2 + \xi_6^2) & 0 & 0 \\ 2\xi_4\xi_5 & -(\xi_4^2 + \xi_6^2) & 0 \\ 2\xi_4\xi_6 & 2\xi_5\xi_6 & -(\xi_4^2 + \xi_5^2) \end{bmatrix}.$$

2.3 NUMERICAL IMPLEMENTATION

According to the Green's second theorem, the boundary integral equation (BIE) can be derived as,

$$\begin{aligned} 2\pi\varphi_d(\vec{x}, t) &= \iint_{\vec{S}_f + \vec{S}_b} \frac{\partial\varphi_d(\vec{x}', t)}{\partial n} G(\vec{x}, \vec{x}')ds - \\ &\iint_{\vec{S}_f + \vec{S}_b} \varphi_d(\vec{x}', t)\frac{\partial G(\vec{x}, \vec{x}')}{\partial n}ds \end{aligned} \tag{22}$$

where $\vec{x} = (x, y, z)$ and $\vec{x}' = (x', y', z')$ are field point and source point, respectively; $\vec{S}_f$ and $\vec{S}_b$ are mean free surface and mean wetted hull. By using the image method, the Green function $G(\vec{x}, \vec{x}')$ can be expressed as,

$$G(\vec{x}, \vec{x}') = \frac{1}{r} + \frac{1}{r'} \tag{23}$$

where,

$$\begin{cases} r = \sqrt{(x - x')^2 + (y - y')^2 + (z - z')^2} \\ r' = \sqrt{(x - x')^2 + (y - y')^2 + (z + z' + 2h)^2} \end{cases} \tag{24}$$

In order to avoid numerical errors due to a direct difference method, the related physical variables are approximately described by quadratic B-spline function,

$$\begin{cases} \varphi_d(\vec{x}, t) \approx \sum_{j=1}^{9}(\varphi_d)_j(t)B_j(\vec{x}) \\ \zeta_d(\vec{x}, t) \approx \sum_{j=1}^{9}(\zeta_d)_j(t)B_j(\vec{x}) \\ \frac{\partial\varphi_d}{\partial z}(\vec{x}, t) \approx \sum_{j=1}^{9}(\partial\varphi_d/\partial z)_j(t)\,B_j(\vec{x}) \end{cases} \tag{25}$$

By submitting Eq. (23) in Eq. (20), a set of linear equations can be obtained according to the distribution of source points on $\vec{S}_b$ and $\vec{S}_f$,

$$\begin{aligned} &2\pi(\varphi_d)_i + \sum_{j=1}^{N_b} Q_{i,j}(\varphi_d)_j - \sum_{j=N_b+1}^{N_b+N_f} P_{i,j}\left(\frac{\partial\varphi_d}{\partial n}\right)_j \\ &= \sum_{j=1}^{N_b} P_{i,j}\left(\frac{\partial\varphi_d}{\partial n}\right)_j - \sum_{j=N_b+1}^{N_b+N_f} Q_{i,j}(\varphi_d)_j \\ &, i = 1\sim N_b \end{aligned} \tag{26}$$

$$\sum_{j=1}^{N_b} Q_{i,j}\,(\varphi_d)_j - \sum_{j=N_b+1}^{N_b+N_f} P_{i,j}\left(\frac{\partial\varphi_d}{\partial n}\right)_j = \sum_{j=1}^{N_b} P_{i,j}\left(\frac{\partial\varphi_d}{\partial n}\right)_j - \sum_{j=N_b+1}^{N_b+N_f} Q_{i,j}\,(\varphi_d)_j - 2\pi(\varphi_d)_i \quad ,i = N_b+1 \sim N_b+N_f \quad (27)$$

where N_b and N_f are the numbers of discretized panels on $\vec{S}_b$ and $\vec{S}_f$ respectively. The detailed evaluation method for the influence coefficients $P_{i,j}$ and $Q_{i,j}$ can be found in Mei et al...

In addition, an artificial damping beach is installed in the kinematic free surface condition to satisfy the radiation condition which can be found in Huang (1997). Also, an artificial spring model by Kim and Kim (2011) should be installed for evaluation of surge motion and added resistance to avoid numerical divergence.

3 EXPERIMENTAL BENCHMARK TESTS

The tests in shallow water were executed using a 1:89.11 scale model of the DTC in the Towing Tank for Manoevres in Confined Water (cooperation FHR and UGent). Eight captive model tests and two tests in free running mode are selected. The details of the experimental setup can be found in Van Zwijnsvoorde et al., (2019), here only the selected benchmark test conditions are listed in Table 1 and Table 2.

For the experimental setup of the DTC container ship in deep water, tests in regular waves have been conducted by MARINTEK (Now SINTEF Ocean), see el Moctar et al. (2015). The presented model test results for deep water in this paper are from Lyu and el Moctar, (2017). Here, the selected test conditions are given in Table 3.

Table 1. Benchmark tests: Captive tests with the bare hull in waves.

Test ID	Velocity		Environment	
	Model scale (m/s)	Full scale (kts)	UKC	λ/L
CW1;CW2;CW3	0;0.327; 0.872	0;6; 16	100%	0.55
CW4;CW5	0;0.327	0;6	20%	0.55

Table 2. Benchmark tests: Free running wave tests.

Test ID	Velocity		Environment	
	Model scale (m/s)	Full scale (kts)	UKC	λ/L
FW1	0.327	6	100%	0.55
FW2	0.872	16	100%	0.40

Table 3. Model tests of the DTC container ship in deep water.

Run	*Fr*	H(m)	T(s)	β(°)
CE4000	0.139	11.3236	15.7628	180
CE4010	0.139	12.5025	15.0429	180
CE4090	0.139	9.463	15.0119	180
CE4100	0.139	6.2325	14.9913	180
CE4241	0.139	9.0174	14.3478	180
CE4251	0.139	6.1649	14.312	180
CE4260	0.139	7.6006	14.2829	180
CE4020	0.139	13.0552	9.9868	180
CE4030	0.139	9.9967	9.0284	180
CE4040	0.139	7.2495	8.0136	180
CE4050	0.139	4.448	7.0066	180
CE4060	0.139	1.5009	5.008	180
CE4070	0.139	0.9966	5.0049	180
CE4080	0.139	0.65	5.0033	180

4 RESULTS AND DISCUSSIONS

The main particulars the Duisburg Test Case (DTC) container ship are listed in Table 4. Due to the symmetry of the numerical field, only half of the computational domain is used. Figure 3 shows the discretized panels on boundaries, where the truncated free surface computational domain is 1.5L upstream, 2L downstream and 0.8L half width. The total number of discretized panels are 4950, where 1200 on half-ship hull and 3750 on half-free surface.

Table 4. Main particulars of DTC

Length (L) (m)	355.0
Breadth (B) (m)	51.0
Draft (T) (m)	14.5
Longitudinal centre of gravity (m)	-2.941
Vertical centre of gravity (m)	19.851
Displacement (m^3)	173467
Block coefficient (C_B)	0.661
Froude number (F_r)	0.139

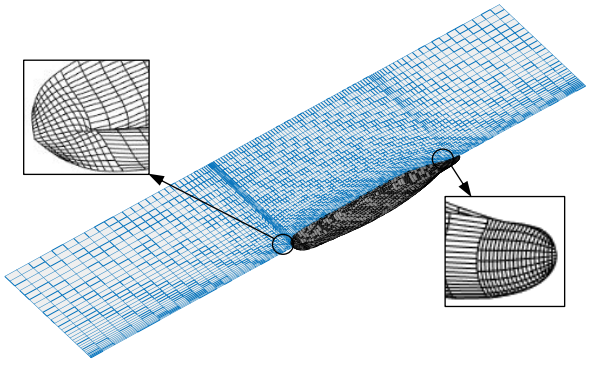

Figure 3. Discretized panels on body and free surface.

4.1 WAVE EXCITING FORCE

Figure 4 shows the time histories of wave exciting force and moment at four water depths, i.e. infinite water depth, 100% UKC, 50% UKC and 20% UKC. As can be seen, all

of the curves are smooth, which demonstrates the good numerical stability of the present program. It's worth noting that, even for the same wave frequency of the incident wave ($\omega_0\sqrt{L/g} = 3.0$), the time history curves at four water depths show different encounter wave frequencies due to the dispersion relation in finite water depth (see Figure 2).

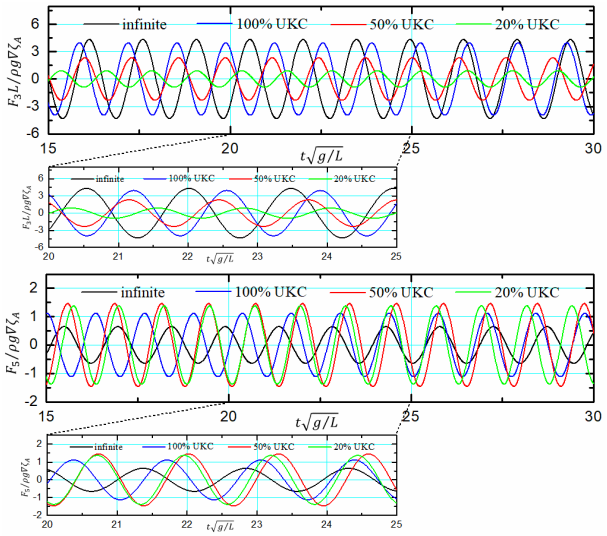

Figure 4. Time histories of wave exciting force and moment at four water depths. Heave force (top), Pitch moment (bottom), $\omega_0\sqrt{L/g} = 3.0$, $F_r = 0.139$.

The non-dimensional wave exciting heave force and pitch moment with respect to frequencies at different water depths are plotted in Figure 5. The amplitudes of frequency results are obtained by using Fourier series expansion from the time history results corresponding to the same frequency. From Figure 5, it can be observed that the obvious difference mainly occurs at low frequencies for four water depths, whereas the values at high frequencies don't show obvious differences except for phase shift persistence. In low frequency areas, the most distinct feature is that the peak values of wave excitation force and moment RAO move toward lower frequencies with decreasing water depth, the same conclusion can also be found in Kim and Kim (2012) for the zero forward speed case by Rankine panel method and in Perunovic and Jensen (2003) for the nonzero forward speed case by strip method. The reason is because the peak value is closely related to the ratio of wave length to the projected length of the ship on the direction of incident wave (i.e. $\lambda/L\cos\beta$).

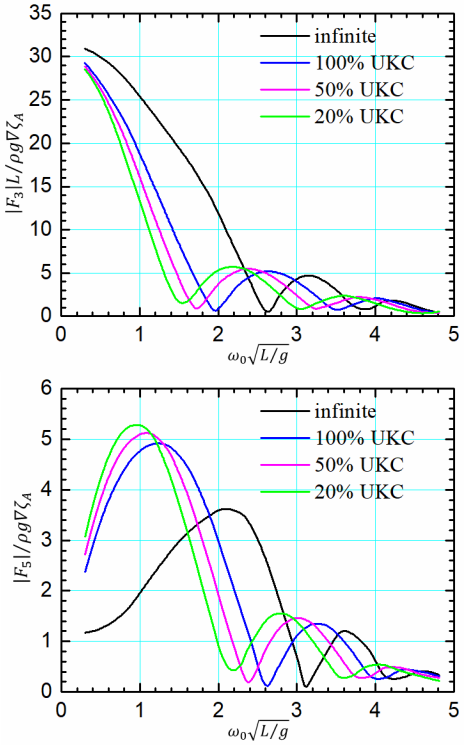

Figure 5. RAO of wave exciting force and moment. Heave force (top), Pitch moment (bottom), $F_r = 0.139$.

4.2 HYDRODYNAMIC COEFFICIENTS

Figure 6 presents the added mass and damping coefficients due to forced heave and pitch motion for different water depths. From the figures in (a) and (c), it can be observed that the added mass decline sharply in low frequencies, while almost tend to flatten with increasing of the frequency; as for the damping coefficients in (b) and (d), the results increased in the dimensionless frequency areas lower than 1.0 and then decreased with the increased frequency. Generally speaking, a shallow water induces larger hydrodynamic coefficients; low frequency incident wave makes enormous contributions to the hydrodynamic coefficients in both deep and shallow water, especially for the added mass, while the results almost converge to the deep-water case with increasing wave frequency. The reason is that the wave length does not change dramatically at high wave frequency areas according to the dispersion relation (see Figure 2). However, the shallow water effect is much more significant. This is because the incident waves are limited by the sea bottom for such low frequency and therefore more energy is needed to accelerate the fluid movement around the ship in the low frequency range in shallow water.

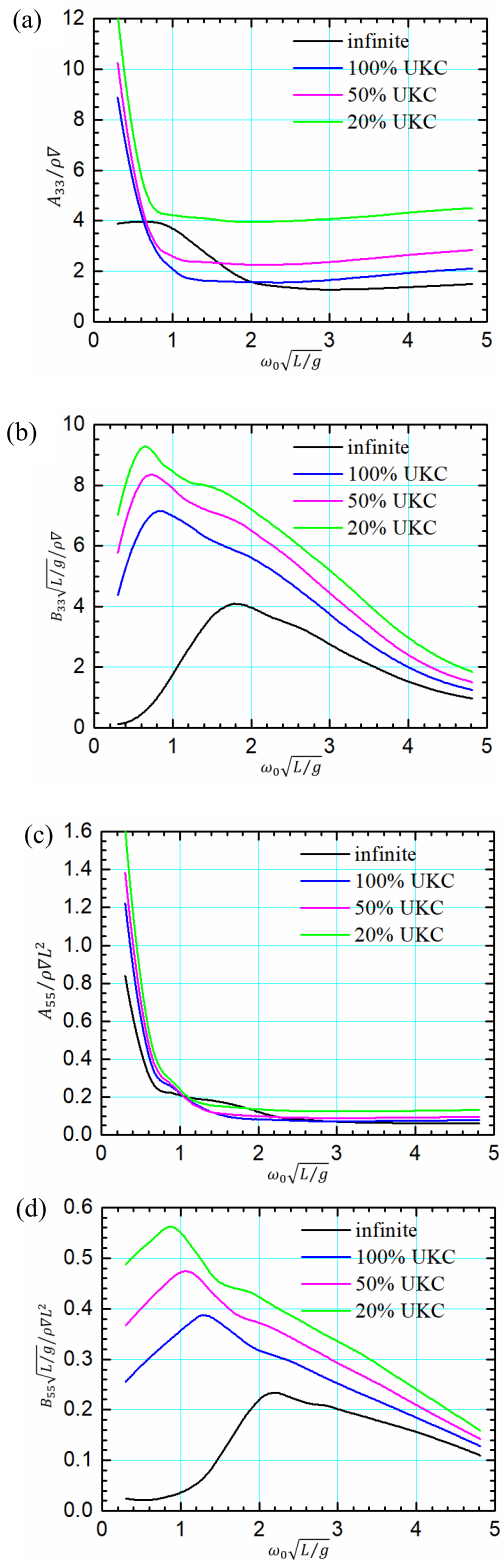

Figure 6. Added mass and damping coefficients. (a), (b) are added mass and damping coefficients due to heave motion; (c), (d) are added mass and damping coefficients due to pitch motion. $F_r = 0.139$.

4.3 MOTIONS IN REGULAR WAVES

Figure 7 shows the time series of heave and pitch motion under four water depths at $\omega_0\sqrt{L/g} = 3.0$, $F_r = 0.139$. Similar to the time histories of wave exciting force in Figure 3, the curves in Figure 7 also show good smoothness and stability. Bear in mind that the wave induced motions show different encounter wave periods even for the same incident wave frequency. The reason is the orbit of a wave fluid particle is strongly dependent on water depth, so in the shallow water, the flow is obstructed by the keel clearance which is different from those of in deep water.

The top figures in Figure 8 (a) and (b) present the comparison of numerical and experimental time history results for heave and pitch motion at $\lambda/L = 0.55$ ($\omega_0\sqrt{L/g} \approx 2.89$) in 100% UKC condition, where the experimental amplitude and numerical amplitude are 0.031m and 1.0m, respectively. As can be seen from experimental time signals, during the experimental process, the acceleration and transition zones exist before the ship reaches a stable state (between two dotted lines), after then, the intended regular wave pattern is disturbed because of reflections by the beach and the wave maker. In addition, due to the significant squat behaviour in shallow water, the mean values of experimental heave and pitch motion time signals (red line) are not zero anymore, which are different from the values calculated by the linear potential method (blue line). However, when the mean values of the experimental time histories in steady state (between two dotted lines) are transformed to zero (see the bottom figures in Figure 8 (a) and (b)), though some phase angle deviations exist due to measurement, a good consistency can be found by comparing with numerical results.

Figure 9 depicts the present numerical results of heave and pitch motion RAO at different water depths, obtained from time series of corresponding wave frequency by Fourier series expansion in comparison with the experimental data. Here, the experimental results in shallow water come from the Towing Tank for Manoeuvres in Confined Water (cooperation FHR and UGent) and the deep water test data and CFD results are obtained from Lyu and el Moctar (2017). As can be seen, generally the numerical results are consistent with experimental data, however some deviations can still be found, especially for heave motion, even for the case in deep water. Similar discrepancies are reported in Lyu and el Moctar (2017) . One reason, as explained in Lyu and el Moctar (2017), might be the pitch resonance which has an influence on heave motions; another reason may be the linear potential method, which does not consider nonlinearities, such as transient wetted surface, being used in this study. Therefore, it is likely that the linear-based Rankine panel method should be extended to a nonlinear one when considering the forward speed seakeeping problem in shallow water.

Figure 10 shows the wave contours around DTC containership at different water depths in regular wave at normalized wave frequency $\omega_0\sqrt{L/g} = 1.98$. It can be seen that the shallower the water depth, the shorter the wavelength at the same wave frequency. This can also be verified in Figure 2.

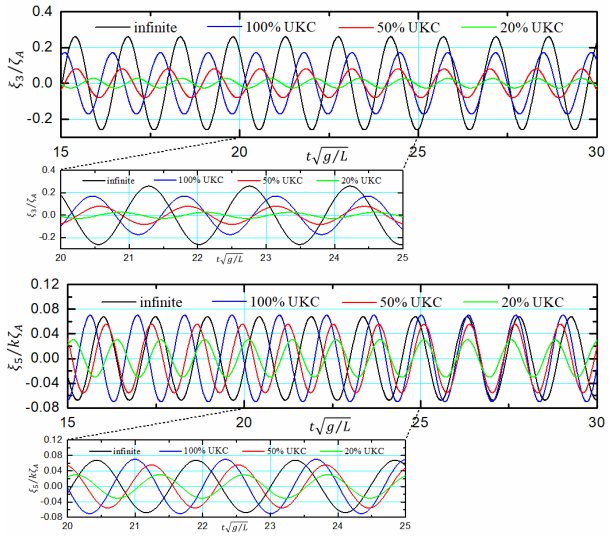

Figure 7. Time histories of heave and pitch motion at four water depths. Heave motion (top), Pitch motion (bottom), $\omega_0\sqrt{L/g} = 3.0$, $F_r = 0.139$.

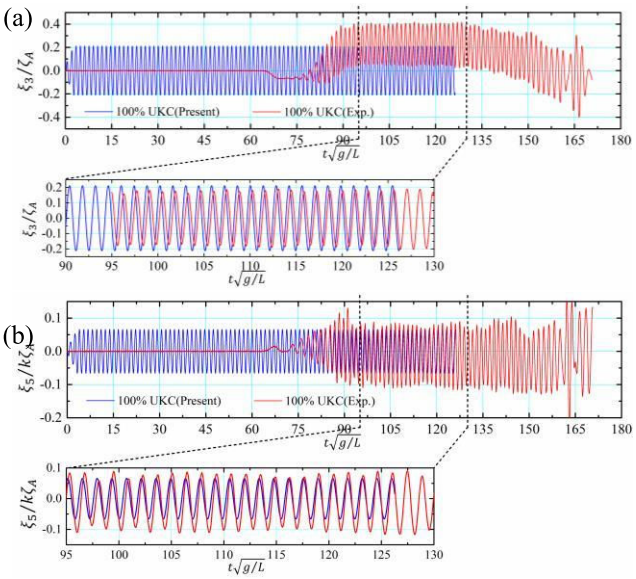

Figure 8. Comparison of numerical and experimental time history results. (a) Heave motion; (b) Pitch motion. $\lambda/L = 0.55$, $F_r = 0.139$.

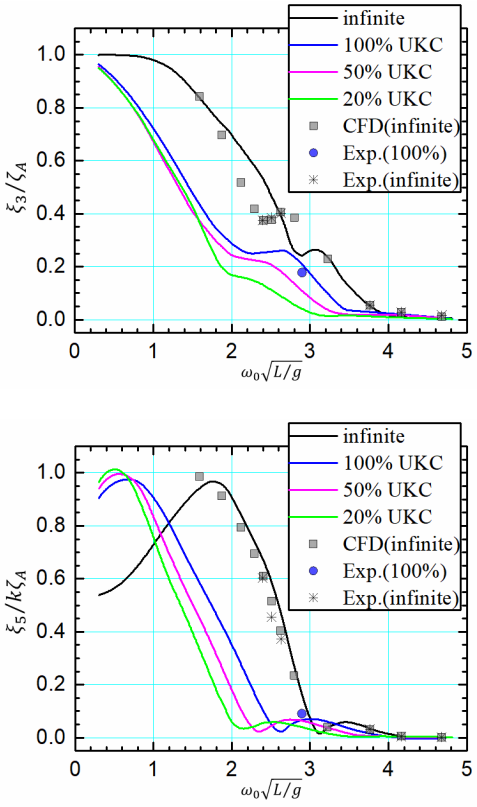

Figure 9. Heave and pitch motion RAO at four water depths. Heave motion RAO (top), Pitch motion RAO (bottom). $F_r = 0.139$.

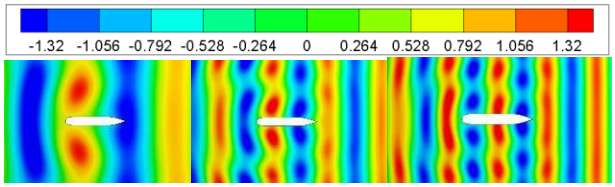

Figure 10. Wave contours around DTC containership at different water depths. Infinite water (left), 100%UKC (middle) and 20%UKC (right). $F_r = 0.139$. $\omega_0\sqrt{L/g} = 1.98$

4.4 ADDED RESISTANCE

Figure 11 presents the time series of the first and second order surge force at three water depths (i.e. infinite water, 100%UKC and 20%UKC), where the second order surge force is obtained by the pressure integration method, as presented in Eq. (21). From the figures, the oscillation period of the second order surge force is almost twice as large as the first order surge force. In addition, the convergence speed of the second order force is slower than the first order, which implies that longer simulation time are needed.

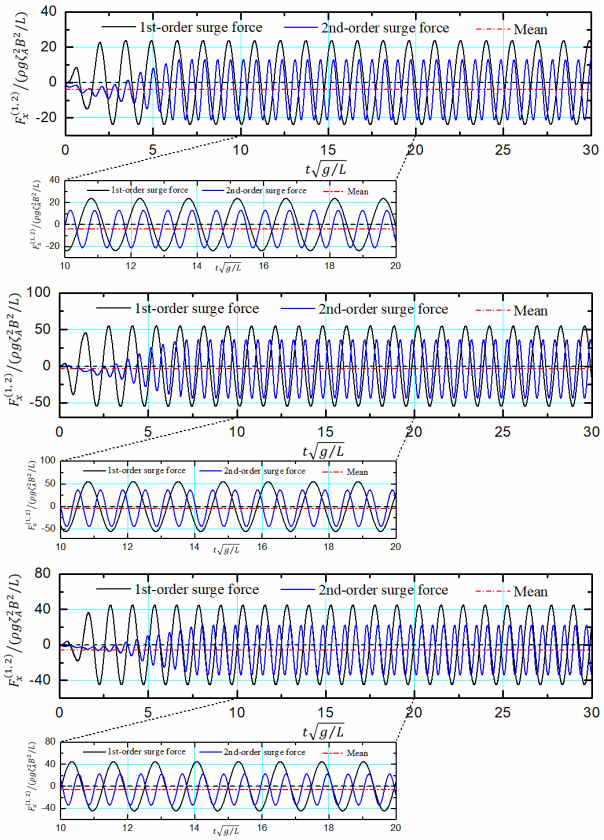

Figure 11. Time histories of added resistance at three water depths. Infinite water (top), 100% UKC (medial) and 20% UKC (bottom), $\omega_0\sqrt{L/g} = 3.0, F_r = 0.139$.

Figure 12 shows the comparisons of added wave resistance at infinite and 100%UKC water depths with experiment data. As can be seen, the normalized added resistance RAO values in infinite water show fair agreement with experimental results, but the values are overestimated in the low wavelength areas. Though some deviations exist, the order of magnitudes between numerical and experimental results for 100%UKC are acceptable. In general, the peak values of numerical added resistance RAO shift toward to lower wave lengths with the decrease of water depth.

In addition, though the numerical values for 100% UKC (Figure 12) and 20% UKC (Figure 13) have a similar trend with the infinite water case, it is not clear to find a consistent trend compared with experiment results, especially for the case in 20% UKC, which is significantly higher than other conditions. The reasons can be explained as follows: on one hand, in fact, the 20% UKC is no more a static condition but a dynamic one for the measurement from the experimental runs; what's more, an issue worth noting in experiment processing is that the incident wave amplitudes should be very small in order to avoid the bottom contact problem in such low under keel clearances, while it is accompanied by measurements and accuracies problems in such an extreme test condition; the detailed explanation can be found in Sprenger et al. (2017). On the other hand, due to the fact that a linear potential method is applied, without considering the obvious squat and viscous effect in shallow water, the numerical accuracy can be questioned as well. Therefore, the effect of water depths on added resistance needs to be further investigated for both numerical and experimental in a future study. Anyway, to an extent, the results can still be used as a qualitative analysis at the initial stages of design.

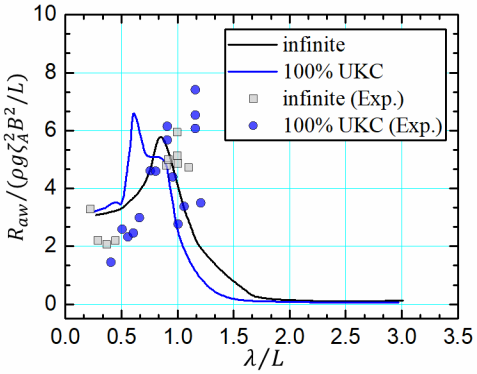

Figure 12. Comparisons of added wave resistance at infinite and 100%UKC water depths. $F_r = 0.139$.

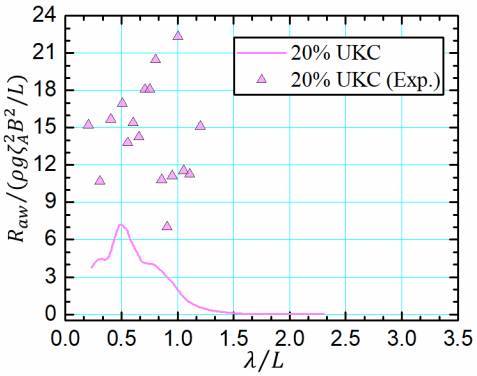

Figure 13. Comparisons of added wave resistance at 20%UKC water depths. $F_r = 0.139$.

5 CONCLUSIONS

In the present study, the wave-body interaction problems, including hydrodynamic forces, motion response and added resistance, is investigated in finite water by using a time domain Rankine panel method. Experimental tests are also carried out to validate the present program. From the results and discussions, the following conclusions can be obtained:

1) Generally, in shallow water larger hydrodynamic coefficients are obtained. Regarding the added mass, lower frequency waves induce larger hydrodynamic coefficients compared to high frequency waves in both deep and shallow water, while the results will converge to the deep-water case with the increasing of wave frequency;

2) The shallower the depth, the larger the peak value of the wave induced force and moment is. Peak values of excitation RAO shift toward to lower frequencies with regard to the decreased water depth; similar results can also be

found for the peak values of heave and pitch motion responses. Through the comparison of numerical results with experimental data for motion responses in different water depths, it can be concluded that the present linear approach is applicable for the prediction of wave body interaction problems related to motion dynamics in shallow water, which also had been proven in Kim and Kim, 2013.

3) As for the added wave resistance, the peak values of added resistance RAO shift toward to lower wave lengths with the decrease of water depth. Though the numerical results in deep water can agree well with test data, it is not clear to find a consistent trend for finite water depths, especially for the extreme test condition (20% UKC). In order to estimate the second order force in shallow water as accurately as possible, it is necessary to extend the present potential method to consider squat and viscous effects.

6 ACKNOWLEDGEMENTS

This work was supported by the Lloyd's Register Foundation (LRF) and China Scholarships Council (CSC). LRF and CSC help to protect life and property by supporting engineering-related education, public engagement and the application of research. The authors acknowledge the contributions of MARINTEK and the Towing Tank for Manoeuvres in Confined Water (cooperation FHR and UGent) with respect to the experimental data for the Duisburg Test Case (DTC) Containership. The authors would also like to thank the SHOPERA (Energy Efficient Safe SHip OPERAtion) consortium and the 5th MASHCON international conference for making available the model test.

7 REFERENCES

Chan, H. S., 1990. A three-dimensional technique for predicting first and second order hydrodynamic forces on a marine vehicle advancing in waves. University of Glasgow, Glasgow, UK.

el Moctar, Sigmund S., Schellin T., 2015. Numerical and experimental analysis of added resistance of ship in waves. In: Proceedings of the ASME 2015 34th International Conference on Ocean, Offshore and Arctic Engineering OMAE 2015, St. John's, NL, Canada.

Feng, A. C., Bai, W., You, Y. X., Chen, Z. M., Price, W. G., 2016. A Rankine source method solution of a finite depth, wave–body interaction problem. Journal of Fluids and Structures, 62: pp. 14-32.

Gao, Z. L., Zou, Z. J., Wang H. M., 2008. Numerical solution of the ship wave-making problem in shallow water by using a high order panel method. Journal of Ship Mechanics, 12 (6): pp. 858-869.

Huang, Y., 1997. Nonlinear ship motions by a Rankine panel method. Massachusetts Institute of Technology, Cambridge, USA, (Ph.D. Thesis).

Hwang, J. H. Lee, S. J., 1975. The effect of forebody forms on the ship motion in water of finite depth. Bulletin of the Society of Naval Architects of Korea, 2(12): pp. 59-66.

Joncquez, S. A. G., 2009. Second-order forces and moments acting on ships in waves. DTU Mechanical Engineering, Denmark. (Ph.D. Thesis).

Kim, C. H., 1968. The influence of water depth on the heaving and pitching motions of a ship moving in longitudinal regular head waves. Schiffstechnik, 15 (79): pp. 127-132.

Kim, Y. H., 1999. Computation of higher-order hydrodynamic forces on ships and offshore structures in waves. Institute of Technology, Massachusetts, USA, (Ph.D. Thesis).

Kim, K. H., Kim, Y., 2011. Numerical study on added resistance of ships by using a time-domain Rankine panel method. Ocean Engineering, 38(13): pp. 1357-1367.

Kim, T. Y., Kim, Y. H., 2012. Numerical study on floating-body motions in finite depth. International Journal of Ocean System Engineering 2(3): pp. 176-184.

Kim, T. Y., Kim, Y. H., 2013. Numerical analysis on floating-body motion responses in arbitrary bathymetry. Ocean Engineering, 62 (4): pp. 123-139.

Li, L., 2001. Numerical seakeeping predictions of shallow water effect on two ship interactions in waves. Dalhousie University, Nova Scotia, Canada. (Ph.D. Thesis).

Lyu, W., el Moctar O., 2017. Numerical and experimental investigations of wave-induced second order hydrodynamic loads. Ocean Engineering, 131: pp. 197-212.

Mei, T. L., Zhang, T., Candries, M., Lataire, E., Zou, Z. J. (2019). Comparative study on ship motions in waves based on two time domain panel methods. Under review.

Perunovic, J. V., Jensen, J. J., 2003. Wave loads on ships sailing in restricted water depth. Marine Structures, 16: pp. 469-485.

Riesner, M., von Graefe, A., Shigunov, V., el Moctar, O., 2016. Prediction of non-linear ship responses in waves considering forward speed effects. Ship Technology Research, 63(3): pp. 135-145.

Riesner, M., el Moctar, O., 2018. A time domain boundary element method for wave added resistance of ships taking into account viscous effects. Ocean Engineering, 162: pp. 290-303.

Söding, H., Shigunov, V., Schellin, T. E., el Moctar, O., 2014. A Rankine panel method for added resistance of ships in waves. Journal of Offshore Mechanics and Arctic Engineering, 136(3).

Sprenger, F., Maron, A., Delefortrie, G., Van Zwijnsvoorde, T., Cura-Hochbaum, A., Lengwinat, A., Papanikolaou, A., 2017. Experimental studies on seakeeping and maneuverability of ships in adverse weather conditions. Journal of Ship Research 61(3): pp. 131-152.

Takaki, M., 1977. On the ship motions in shallow water (Part 3): Comparison of the experimental results with the calculated results of ship motions in waves. Transactions of the West Japan Society of Naval Architects, 54: pp. 103-114.

Takaki, T., Takaki, M., Ohkusu, M., 1978. Ship motions in restricted waters. Transactions of the West Japan Society of Naval Architects, 56: pp. 33-45.
Andersen, P., 1979. Ship motions and sea loads in restricted water depth. Ocean Engineering, 6(6): pp. 557-569.

van Oortmerssen, G., 1976. The motions of a ship on shallow water. Ocean Eng. 3: pp. 221-255.

Vantorre, M., Journée, J., 2003. Validation of the strip theory code SEAWAY by model tests in very shallow water. In Colloquium on Numerical Modelling: pp. 23-24.
Tuck, E. O., 1970. Ship motions in shallow water, J. Ship Res. 14 (4): pp. 317-328.

Van Zwijnsvoorde, T., Tello Ruiz, M., Delefortrie G., Lataire E., 2019. Sailing in shallow water waves with the DTC container carrier: open model test data for validation purposes. In: Proceedings of 5th MASHCON International Conference on Ship Manoeuvring in Shallow and Confined Water, Ostend, Belgium.

Vorobyov, Y. L., Stasenko M. S., 2010. Asymptotic theory of ship motions in regular waves under shallow water conditions. Transnav the International Journal on Marine Navigation and Safety of Sea Transportation, 4(4): pp. 415-420.

Wang, L. X., Tang, H., Wu, Y. H., 2016. Wave interaction with a surface-piercing body in water of finite depth: a parametric study. Engineering Applications of Computational Fluid Mechanics, 10(1): pp. 514-530.

Yao, C. B., Sun, X. S., Wang W., Ye Q., 2017. Numerical and experimental study on seakeeping performance of ship in finite water depth. Applied Ocean Research, 67: pp. 59-77.

8 AUTHORS BIOGRAPHY

Tianlong Mei, PhD student at School of Naval Architecture, Ocean and Civil Engineering, Shanghai Jiao Tong University and the division of Maritime Technology at Ghent University. His experience includes numerical studies on wave structure interaction and ship manoeuvring in waves.

Guillaume Delefortrie, PhD, naval architect, is expert nautical researcher at Flanders Hydraulics Research and visiting professor at Ghent University. He is in charge of the research in the Towing Tank for Manoeuvres in Confined Water and the development of mathematical models based on model tests. He has been secretary of the 27th and 28th ITTC Manoeuvring Committee and is chairman of the 29th ITTC Manoeuvring Committee.

Manasés Tello Ruiz, PhD, naval architect and marine engineer, is a researchs at Ghent University. He has been involved in several (inter)national projects with main focus on manoeuvring, seakeeping, and wave energy converters. Currently, he is working on ship air pollution and machine learning techniques applied to ship hydrodynamics. At present he is also a member of the ITTC Specialist Committee of Manoeuvring in Waves, at which he has been appointed as secretary..

Changyuan Chen, a PhD candidate at the Maritime Technology Division, which belongs to the Faculty of Engineering and Architecture of Ghent University. His experience includes research on trajectory controller, intelligent control strategies, machine learning techniques applied to ship hydrodynamics, etc.

Evert Lataire, PhD, naval architect, is currently post-doctoral assistant at the division of Maritime Technology at Ghent University. He has written a PhD on the topic of bank effects mainly based upon model tests carried out in the shallow water towing tank of FHR. His fifteen year experience includes research on ship manoeuvring in shallow and confined water such as ship-ship interaction, ship-bottom interaction and ship-bank interaction.

Marc Vantorre, naval architect, is full senior professor of marine hydrodynamics and head of the Maritime Technology Division at Ghent University, Belgium. His research focuses on ship behaviour in shallow and confined waters, mainly in close co-operation with Flanders Hydraulics Research in Antwerp. He is member of PIANC Working Groups and former member of the ITTC Manoeuvring Committee. The investigation of manoeuvring behaviour in muddy areas has been a topic throughout his career.

Zaojian Zou, holds the current position of full professor at School of Naval Architecture, Ocean and Civil Engineering, Shanghai Jiao Tong University. He is responsible for teaching and research on marine hydrodynamics. His previous experience includes PI of some projects on manoeuvring and control of ships and other marine vehicles. He was a member of the 22nd, 23rd, 25th and 26th ITTC MC.